Inorganic Chemistry
Cite This: Inorg. Chem. XXXX, XXX, XXX–XXX
Article
pubs.acs.org/IC

Hydrogen Atom Abstraction by High-Valent Fe(OH) versus Mn(OH) Porphyrinoid Complexes: Mechanistic Insights from Experimental and Computational Studies

Jan Paulo T. Zaragoza,[†] Daniel C. Cummins,[†] M. Qadri E. Mubarak,[‡] Maxime A. Siegler,[†] Sam P. de Visser,*[,‡] and David P. Goldberg*[,†]

[†]Department of Chemistry, The Johns Hopkins University, 3400 North Charles Street, Baltimore, Maryland 21218, United States
[‡]The Manchester Institute of Biotechnology and Department of Chemical Engineering and Analytical Science, The University of Manchester, 131 Princess Street, Manchester M1 7DN, United Kingdom

Supporting Information

ABSTRACT: High-valent metal-hydroxide species have been implicated as key intermediates in hydroxylation chemistry catalyzed by heme monooxygenases such as the cytochrome P450s. However, in some classes of P450s, a bifurcation from the typical oxygen rebound pathway is observed, wherein the $Fe^{IV}(OH)$(porphyrin) species carries out a net hydrogen atom transfer reaction to form alkene metabolites. In this work, we examine the hydrogen atom transfer (HAT) reactivity of $Fe^{IV}(OH)$(ttppc) (**1**), ttppc = 5,10,15-tris(2,4,6-triphenyl)-phenyl corrole, toward substituted phenol derivatives. The iron hydroxide complex **1** reacts with a series of *para*-substituted 2,6-di-*tert*-butylphenol derivatives (4-X-2,6-DTBP; X = OMe, Me, Et, H, Ac), with second-order rate constants k_2 = 3.6(1)−1.21(3) × 10^4 M^{-1} s^{-1} and yielding linear Hammett and Marcus plot correlations. It is concluded that the rate-determining step for O−H cleavage occurs through a concerted HAT mechanism, based on mechanistic analyses that include a KIE = 2.9(1) and DFT calculations. Comparison of the HAT reactivity of **1** to the analogous Mn complex, $Mn^{IV}(OH)$(ttppc), where only the central metal ion is different, indicates a faster HAT reaction and a steeper Hammett slope for **1**. The O−H bond dissociation energy (BDE) of the M^{III}(HO−H) complexes were estimated from a kinetic analysis to be 85 and 89 kcal mol^{-1} for Mn and Fe, respectively. These estimated BDEs are closely reproduced by DFT calculations and are discussed in the context of how they influence the overall H atom transfer reactivity.

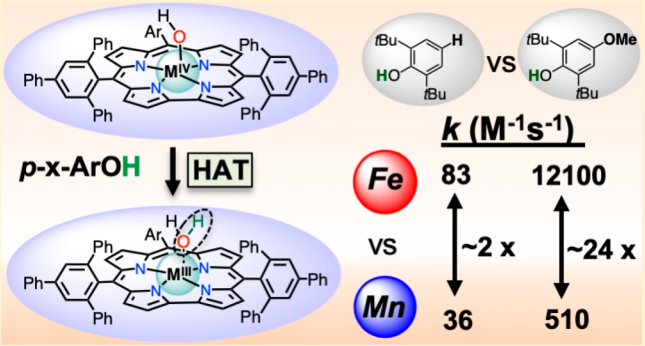

INTRODUCTION

The design and development of well-defined, observable synthetic models of highly reactive metal−oxygen intermediates has helped elucidate the mechanisms of oxidation reactions catalyzed by metalloenzymes.[1,2] For example, synthesis of biomimetic high-valent metal-oxo complexes and examination of their hydrogen atom transfer (HAT) reactivity has provided insights into the ground-state thermodynamics of related biological oxidations, as well as information for the design of synthetic catalysts.[3−7] Heme enzymes are biological catalysts that perform a large variety of oxidation reactions in nature. Cytochrome P450 (CYP), in particular, is a heme monooxygenase that activates inert C−H bonds via a high-valent iron-oxo intermediate, Compound I (Cpd-I).[8−13] The rate-determining step for this reaction is the HAT from the C−H substrate to Cpd-I to form protonated Compound II (Cpd-II), an iron(IV)-hydroxide species (Scheme 1). The subsequent step, which is rapid, is the rebound of the •OH group to the incipient carbon radical to form the hydroxylated substrate. Indeed, many of the studies of HAT involving model systems have focused on the reactivity of metal-oxo complexes and the thermodynamic analysis of the O−H bond of the metal-hydroxide intermediate formed during the HAT reaction. However, CYP monooxygenases, and the related CYP peroxygenases, can perform desaturation and C−C bond cleaving reactions in addition to hydroxylation, where their pathways can bifurcate at the Cpd-II state between oxygen rebound and HAT mechanisms. Desaturation reactions result in the formation of toxic alkene metabolites (Scheme 1). Conversion of valproic acid to 4-ene valproic acid,[14−16] ethyl carbamate to vinyl carbamate,[17] testosterone to 17β-hydroxy-4,6-androstadiene-3-one,[18] lauric acid to 11-dodecenoic acid,[19] and decarboxylation of fatty acids to terminal alkenes (specifically by $OleT_{JE}$)[20−25] are just some of the examples of these CYP-mediated desaturation reactions.

While substrate positioning in the active site binding pocket has been implicated to play a key role in selection of rebound

Received: October 1, 2019

DOI: 10.1021/acs.inorgchem.9b02923
Inorg. Chem. XXXX, XXX, XXX–XXX

Scheme 1. Divergent Oxidation Pathways for CYP Cpd-II, and Examples of Desaturation Reactions Mediated by CYPs

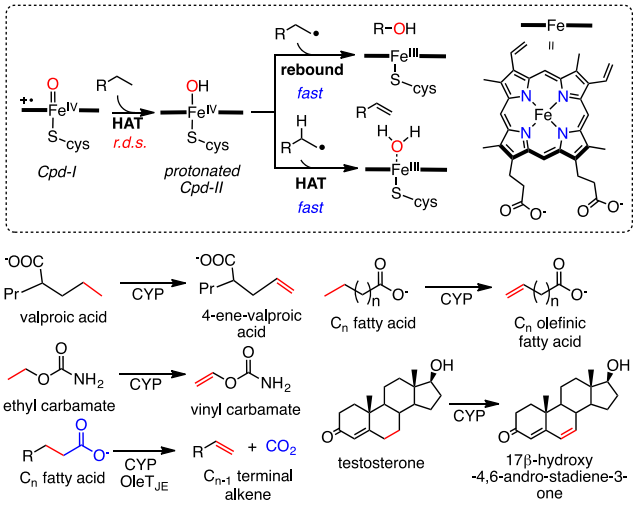

hydroxylation versus HAT pathways for protonated Cpd-II in CYPs,[22,26] the fundamental electronic and structural factors that ultimately control these pathways remain poorly understood. Ground state thermodynamic properties are often invoked as key factors in controlling HAT by high-valent metal-oxo complexes. Along these lines, the ground state thermodynamics related to the HAT reactivity of protonated Cpd-II can be assessed from the BDE(O−H) of the expected ferric-aquo product ($Fe^{III}(H_2O)$(porph)(cys)). Few such BDE values are available from experiment on heme enzymes, but a BDE(O−H) of 90 kcal mol^{-1} was recently reported in one case for the $Fe^{III}(H_2O)$ species in CYP158.[27] In contrast, the $Fe^{III}(H_2O)$ form of the heme enzyme aromatic peroxygenase (APO) was characterized as having a much lower BDE of 81 kcal/mol, despite the similarity of this thiolate-ligated heme active site with that of Cys-bound CYP. The corresponding O−H bond strength in the ferric hydroxide form of horseradish peroxidase (HRP), which contains a neutral His axial ligand *trans* to the OH group, is 85 kcal/mol as derived from the $Fe^{IV}(O)/Fe^{III}(OH)$ redox potential.[28] Such a wide range in similar porphyrin ferric O−H bond strengths indicates that there are likely subtle, as yet unidentified factors regarding the metal ion active site that can affect this value and ultimately influence HAT reactivity.

Given the challenges in characterizing these species in the native, enzymatic systems, we have set out to develop well-defined synthetic $Fe^{IV}(OH)/Fe^{III}(H_2O)$ porphyrinoid complexes that should allow for an examination of their reactivity and related thermodynamics. Such compounds, in heme or nonheme systems, are extremely rare. We previously reported the synthesis of $Fe^{IV}(OH)$(ttppc) (ttppc = 5,10,15-tris(2,4,6-triphenyl)-phenyl corrole) (**1**) and its reactivity toward *para*-X substituted trityl radical derivatives in efforts to model the radical rebound step leading to C−O bond formation.[29] Kinetic studies indicated that the radical rebound step was a concerted, charge neutral process. It should be noted that with triarylcorrole ligands, the electronic ground state of formally Fe^{IV} and Mn^{IV} corroles has been described as varying between the two canonical valence tautomers, $M^{III}(X)$(corrole$^{+\bullet}$) and $M^{IV}(X)$(corrole), depending on the axial ligand X.[30,31] Conclusive characterization of the ground electronic state of these compounds is challenging, and complex **1** and the analogous Mn(OH)(ttppc) will be described as metal(IV) hydroxide complexes throughout this work for simplicity. Since our original report, the complex $Fe^{IV}(OH_n)$(TAML) (TAML = tetra-amido macrocyclic ligand) was reported,[32] as well as a nonheme $Fe^{III}(OH)$ complex that demonstrated both radical rebound and hydrogen atom transfer reactivity.[33]

Herein, the H atom transfer reactivity of $Fe^{IV}(OH)$(ttppc) (**1**) with a series of phenol derivatives is described, providing a mechanistic analysis of HAT reactivity. The synthesis and structural characterization of $Fe^{III}(H_2O)$(ttppc) (**2**), the corresponding HAT product, was also accomplished. Hammett and Marcus plot analyses, together with kinetic isotope effect (KIE) measurements, provide detailed insight into how the HAT reaction proceeds. A direct comparison with the reactivity of $Mn^{IV}(OH)$(ttppc), combined with computational analyses of the reaction trajectories of these two high-valent metal hydroxide complexes, enabled assessment of how the central metal ion (Mn vs Fe) tunes the H atom transfer reactivity. The experimental and computational studies on **1**, along with work on the analogous Mn complex $Mn^{IV}(OH)$-(ttppc), provide novel insights into the thermodynamic properties that govern the reactivity of metal hydroxide species toward H atom donors.

RESULTS AND DISCUSSION

Synthesis and Structural Characterization of an $Fe^{III}(H_2O)$ Complex. The synthesis of $Fe^{III}(H_2O)$(ttppc) (**2**), the expected H atom abstraction product of $Fe^{IV}(OH)$-(ttppc) (**1**), was prepared by ligand exchange of the previously synthesized $Fe^{III}(OEt_2)_2$(ttppc)[29] with H_2O, followed by fluorobenzene/*n*-pentane vapor diffusion to give single crystals for X-ray diffraction. The molecular structure of $Fe^{III}(H_2O)$-(ttppc) (**2**) is shown in Figure 1. The structure of **2** shows an

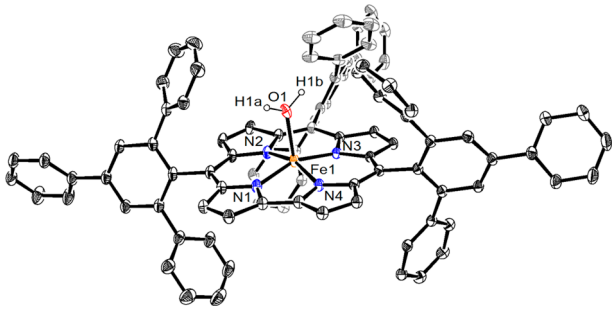

Figure 1. Displacement ellipsoid plot (35% probability level) for $Fe^{III}(H_2O)$(ttppc) (**2**) at 110(2) K. H atoms (except for those attached to O1) are omitted for clarity.

Fe−O bond distance of 2.126(2) Å, which is much longer as compared to that of **1** (Fe−O = 1.857(3) Å, Table S1). The Fe−O bond distance for **2** is similar to other well-characterized mononuclear $Fe^{III}(H_2O)$ units in porphyrin (2.012(2)−2.084(4) Å)[34−36] and tetra-amido macrocyclic ligand scaffolds (TAML) (2.097(2)−2.1102(18) Å).[37,38] The X-ray structure of **2** is the first example of an H_2O-bound iron(III) corrole, which are typically isolated with NO, Et_2O, or pyridine axial ligands.[10−12] The frozen solution EPR spectrum of **2** shows an intense signal at g = 4.29 consistent with an intermediate spin (S = 3/2) Fe^{III} metal center, similar to $Fe^{III}(OEt_2)_2$(ttppc) in toluene (Figure S1)[29] and the related $Fe^{III}(OEt_2)_2$(tpfc) (tpfc = 5,10,15-tris(pentafluorophenyl) corrole).[39,40] An Evans method measurement of **2** gives μ_{eff} = 3.6(1) μ_B, (spin-only

DOI: 10.1021/acs.inorgchem.9b02923
Inorg. Chem. XXXX, XXX, XXX−XXX

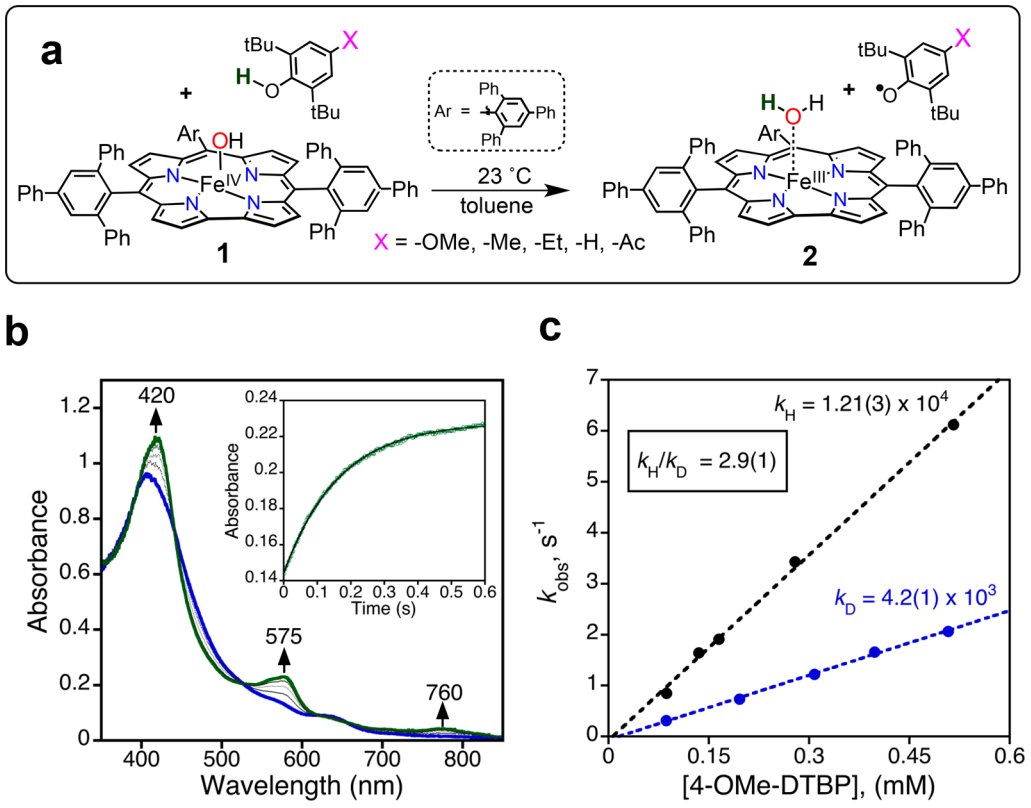

Figure 2. (a) Reaction of Fe^{IV}(OH)(ttppc) with *para*-X-substituted 2,6-di-*tert*-butylphenol derivatives. (b) Time-resolved UV−vis spectral changes observed in the reaction of **1** (15 μM) with 4-OMe-2,6-DTBP (0.52 mM) in toluene at 23 °C. Inset: changes in absorbance vs time for the growth of **2** (575 nm) (green circles) with the best fit line (black). (c) Plot of pseudo-first-order rate constants (k_{obs}) vs [4-OMe-2,6-DTBP] for the OH (black) and OD (blue) phenol isotopologues.

μ_{eff} = 3.87 μ_B for S = 3/2), further supporting the spin state assignment. It should be noted that we are not able to unambiguously determine the extent to which H_2O remains coordinated for the EPR and Evans method measurements in toluene. For comparison, the analogous $Mn^{III}(H_2O)$(ttppc)[41] has a much longer metal−oxygen bond distance of 2.2645(18) Å, likely due to Jahn−Teller distortion for the high-spin Mn^{III} ion.[42]

Reaction of Fe^{IV}(OH)(ttppc) (1) with H Atom Transfer Reagents. Initial studies on the HAT reactivity of **1** began with C−H substrates. Reaction of **1** with 9,10-dihydroanthracene (DHA), a common H atom donor with a relatively weak C−H bond (BDE = 76.3 kcal mol^{-1}),[43] was carried out. Preliminary UV−visible spectroscopy measurements showed that **1** reacts with DHA in toluene at 23 °C, although the reaction is very slow (<5% decay to $Fe^{III}(H_2O)$(ttppc) (**2**) over 5 h). In contrast, reaction of **1** with 2,4-di-*tert*-butylphenol (2,4-DTBP) (toluene, 23 °C) results in rapid formation of **2**, as observed by UV−vis spectroscopy. Product analysis by gas chromatography (GC-FID) led to detection of the bis(phenol) dimer product 3,3′,5,5′-tetra-*tert*-butyl-(1,1′-biphenyl)-2,2′-diol in good yield (67(1)%), consistent with a 1:1 stoichiometry for oxidation of the phenol substrate by the iron complex **1**.

Having demonstrated the proficiency of **1** in cleaving the phenolic O−H bond in 2,4-DTBP, we employed a series of *para*-substituted 2,6-di-*tert*-butylphenol derivatives (4-X-2,6-di-*t*-Bu-C_6H_2OH; X = OMe, tBu, Et, Me, H, Ac) as H atom transfer substrates. Variation of the *para* substituents allowed us to measure the influence of the electronic and thermodynamic properties of the phenol derivatives on the H atom transfer reactivity (Figure 2a). A direct comparison with the reactivity of Mn^{IV}(OH)(ttppc) can also be made, providing an opportunity to assess how the central metal ion (Mn vs Fe) affects the reactivity toward hydrogen atom donors. Reaction of **1** with a series of *para*-substituted phenols were carried out similarly to the reaction of **1** with 2,4-DTBP. A solution of **1** and excess 4-methoxy-2,6-di-*tert*-butylphenol (4-OMe-2,6-DTBP) (5.4 equiv) was analyzed by X-band electron paramagnetic resonance (EPR) spectroscopy (16 K) and gave EPR signals corresponding to $Fe^{III}(H_2O)$(ttppc) (**2**) (g = 4.29) and phenoxyl radical (g = 2.0) (Figure S3a). An additional signal (g = 5.3) appears in this reaction mixture, which can also be observed in the EPR spectrum of $Fe^{III}(H_2O)$(ttppc) (**2**) and excess 4-OMe-2,6-DTBP (possibly due to formation of an Fe^{III}-phenol adduct) (Figure S3b). These data showed that **1** reacts with 4-OMe-2,6-DTBP in accordance to the scheme in Figure 2a. The reaction kinetics of **1** with 4-OMe-2,6-DTBP was monitored by stopped-flow UV−vis spectroscopy, showing isosbestic conversion of **1** to **2** within 1 s (Figure 2b). Pseudo-first-order conditions (>10-fold equiv substrate) were employed and led to single exponential curves that were fit up to five half-lives. The resulting observed rate constant (k_{obs}) varied linearly with phenol concentration, yielding a second-order rate constant (k_2) of 1.21(3) × 10^4 M^{-1} s^{-1}. A kinetic isotope effect (KIE) was determined by reaction of **1** with the ArOD isotopologue of 4-OMe-2,6-DTBP. A KIE of 2.9(1) was measured, indicating that the rate-determining step involves O−H cleavage.

DOI: 10.1021/acs.inorgchem.9b02923
Inorg. Chem. XXXX, XXX, XXX−XXX

The second-order rate constants (k_2) for the other *para*-substituted 2,6-DTBP derivatives were obtained in a similar fashion (Figures S4–S9) and are listed in Table 1 together with their thermodynamic parameters (Hammett constants σ^+_p, redox potentials, and BDEs). It should be noted that the E_{ox} values listed in Table 1 were obtained in acetonitrile. However, we still obtain a good correlation between our measured k_2 values in toluene and the E_{ox} values from CH_3CN. In each case, isosbestic conversion of **1** to the $Fe^{III}(H_2O)$ product **2** was rapid and varied over two orders of magnitude (k_2 = 3.6(1)–1.21(3) × 10^4 M^{-1} s^{-1}).

Table 1. Second-Order Rate Constants for the Reaction Between $Fe^{IV}(OH)$(ttppc) (1) and *para*-X-Substituted Phenol Derivatives, Hammett Constants (σ^+_p), Redox Potentials (E_{ox}), and BDEs of 4-X-2,6-DTBP

X	k_2 (M^{-1} s^{-1})	σ^+_p [a]	E_{ox} [b] (V vs $Fc^{+/0}$)	BDE [c] (kcal mol^{-1})
−OMe	1.21(3) × 10^4	−0.78	0.53	78.3
−OMe (OD)	4.2(1) × 10^3	–	0.59	–
−Me	2.0(1) × 10^3	−0.31	0.81	81.0
−Et	3.2(3) × 10^3	−0.29	0.88	–
−H	83(3)	0.00	1.07	82.8
−Ac	3.6(1)	–	–	84.4

[a]Ref 44. [b]In CH_3CN, ref 45. [c]In benzene, ref 46.

Comparison of the Reactivity of $Fe^{IV}(OH)$(ttppc) (1) and $Mn^{IV}(OH)$(ttppc) with Phenol Derivatives. Hammett analysis of the kinetic data for **1** (Figure 3a, red circles) showed a decrease in the rate constants with the more electron-deficient phenol, with a slope of ρ^+ = −2.6(8). This slope is higher as compared to that of $Mn^{IV}(OH)$(ttppc) (ρ^+ = −1.4(2)) (Figure 3a, blue circles), implying a relatively greater charge separation in the HAT transition state for the Fe versus the Mn complex. A Marcus plot analysis, which provides information on the involvement of electron transfer in the rate-determining step of the reaction, was also performed. A slope of approximately −0.5 is predicted for the plot of (RT/F) ln k_2 versus E_{ox} (where k_2 is the second-order rate constant and E_{ox} is the redox potential of the substrate being oxidized) for reactions with a rate-determining electron transfer step, provided that $\Delta G^\circ_{ET}/\lambda$ (where λ is the reorganization energy) is close to zero.[47] A slope of −0.19(6) was obtained for **1** (Figure 3b, red squares), close to the values obtained for HAT reactions of a Cu-superoxo complex (slope = −0.29)[45] and $Mn^{IV}(OH)$(ttppc) (slope = −0.12) (Figure 3b), in which a concerted H atom transfer is invoked. Plotting the log k_2 for **1** versus the bond dissociation energy (BDE) of the O–H bond of the phenol substrate (Figure 3c) also shows a good correlation, with a slope of −0.58(1). This slope is larger than that for $Mn^{IV}(OH)$(ttppc) (slope = −0.25(3)), suggesting that the $Fe^{IV}(OH)$ complex is more sensitive to the changes in BDEs of the O–H bond being broken. However, it must be noted that the range of BDEs for the O–H substrates is small, and therefore, caution must be used in the interpretation of these data.

The difference in slope implies that $Mn^{IV}(OH)$(ttppc) will exhibit larger rate constants than **1** when reacting with O–H substrates having sufficiently high BDEs (>ca. 85 kcal mol^{-1}). A similar reversal in relative rate of HAT for a nonheme $Mn^{IV}(O)$ versus an analogous $Fe^{IV}(O)$ complex was recently described.[55–57] Taken together, the data suggest a rate-limiting H atom transfer reaction for complex **1** with phenolic (O–H bond) substrates. It is reasonable to conclude that the HAT reaction proceeds in a concerted manner but with a partial transfer of charge, rather than stepwise PT/ET or ET/PT pathways.

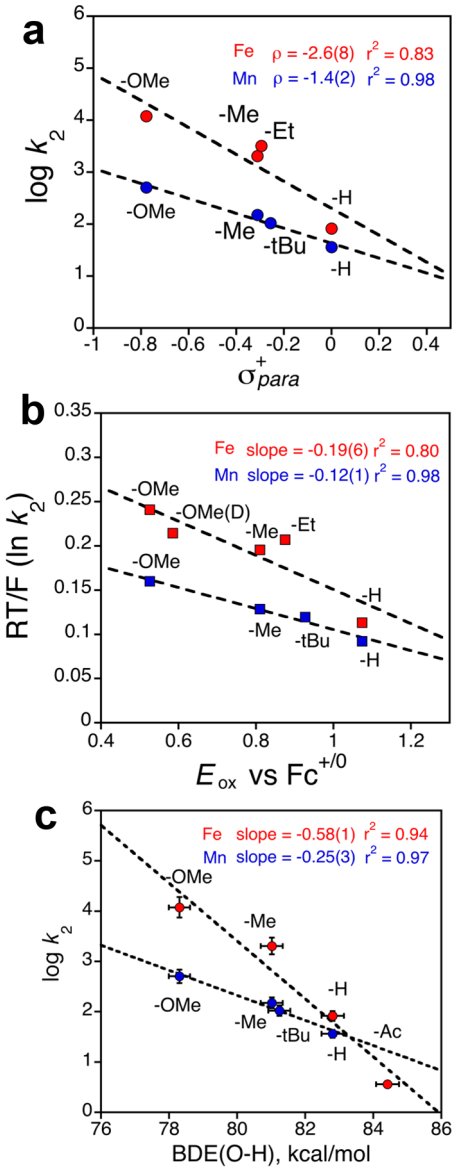

Figure 3. Comparison of (a) Hammett, (b) Marcus, and (c) log k_2 vs BDE plots for the reaction of $Fe^{IV}(OH)$(ttppc) (**1**) (red circles/squares, in toluene) or $Mn^{IV}(OH)$(ttppc) (blue circles/squares, in benzene) with 4-X-2,6-DTBP. Kinetic data for $Mn^{IV}(OH)$(ttppc) from ref 41.

Comparison of HAT Reactivity with Other Oxidants and Estimation of BDEs from the Kinetics Data. The rate constants for the oxidation of 4-X-2,6-DTBP (X = OMe, Me, H) by $Fe^{IV}(OH)$(ttppc) (**1**) and $Mn^{IV}(OH)$(ttppc) can be compared to the previously reported rate constants for substituted phenol oxidation by various metal-oxo and metal-hydroxo complexes, as well as a photolytically generated *t*-BuO• radical (Table 2).[48,50,58] It should be noted that the rate constants in Table 2 are taken from reactions in different solvents and temperatures, and thus close comparisons of the values are not warranted. However, in general, the rate

DOI: 10.1021/acs.inorgchem.9b02923
Inorg. Chem. XXXX, XXX, XXX–XXX

Table 2. Comparison of Second-Order Rate Constants (M^{-1} s^{-1}) and Hammett Slopes (ρ^+) for the Oxidation of Substituted Phenols, 4-X-2,6-DTBP (X = OMe, Me, H), by M(O(H)) Complexes and t-BuO•, and the Corresponding O−H BDEs of the Reduced Complex

oxidant	−OMe	−Me	−H	ρ^+	conditions	reduced complex	BDE (O−H) (kcal mol^{-1})
$Fe^{IV}(OH)(ttppc)$ (**1**)	1.21×10^4	2.0×10^3	83.0	−2.6	toluene, 23 °C	$Fe^{III}(HO{-}H)(ttppc)$	89[a]
$Mn^{IV}(OH)(ttppc)$[b]	510	150	36	−1.4	benzene, 23 °C	$Mn^{III}(HO{-}H)(ttppc)$	85[a]
$Mn^{III}(OH)(dpaq)^+$[c]	1.44	1.20	0.75	−0.88	CH_3CN, 50 °C	$Mn^{II}(HO{-}H)(dpaq)^+$	64[d]
$Fe^{IV}(O)(TMC)(NCCH_3)^+$[e]	11.4	0.18	0.04	−3.20	CH_3CN, 25 °C	$Fe^{III}(O{-}H)(TMC)(NCCH_3)^+$	78[e]
$Fe^{IV}(O)(TMC)(CF_3CO_2)$[e]	26.4	1.84	0.46	−2.30	CH_3CN, 25 °C	$Fe^{III}(O{-}H)(TMC)(CF_3COO)$	76.4[e]
$Fe^{IV}(O)(TMC)(N_3)$[e]	29.8	1.84	0.68	−1.50	CH_3CN, 25 °C	$Fe^{III}(O{-}H)(TMC)(N_3)$	77.4[e]
$Mn^{IV}(OH)(salen)$[f]	–	412	37.3	–	CH_2Cl_2, −70 °C	$Mn^{III}(HO{-}H)(salen)$	–
$[Ru^{VI}(L)(O)_2]^{2+}$[g]	2.56×10^4	26	0.58	−2.90	CH_3CN, 25 °C	$[Ru^{V}(L)(O)(O{-}H)]^{2+}$	82.8[g]
t-BuO•[h]	–	1.2×10^8	4.3×10^7	–	1:2 $C_6H_6/C_8H_{18}O_2$, 22 °C	t-BuO−H	105[i]

[a]BDE values extrapolated from the correlation in Figure 4. BDE(O−H) refers to the bond dissociation energy of the reduced complex. [b]Rate constants from ref 41. [c]Rate constants calculated from k_{obs} (s^{-1}) in ref 48. [d]Ref 49. [e]Rate constants calculated from k_{obs} (s^{-1}) values in ref 50. [f]Rate constants calculated from k_{obs} (s^{-1}) values ref 51. [g]Ref 52. [h]Ref 53. [i]Ref 54.

constants for **1** are orders of magnitude larger than those for Mn- and Fe-oxo and hydroxo complexes. Although the high-valent Fe^{IV}(oxo) complexes in Table 2 may be among the weaker $Fe^{IV}(O)$ oxidants, it is still interesting to note that **1**, a terminal hydroxide complex, is a significantly more reactive oxidant for the electron-rich phenols.

An Evans−Polanyi plot (Figure 4) shows good correlation of the 4-Me-2,6-DTBP reaction rates of these complexes with the

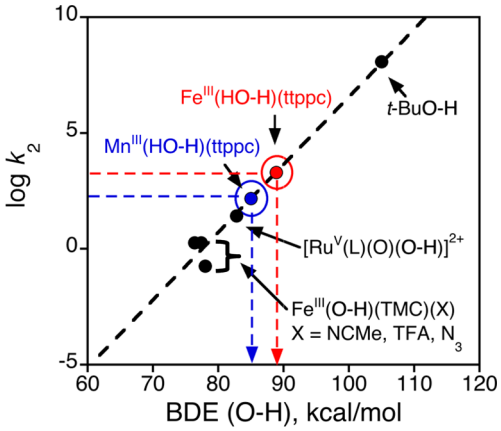

Figure 4. Plot of log k_2 for the reaction of metal-oxo/hydroxo complexes and tBuO• with 4-Me-2,6-*t*-Bu-phenol (22−25 °C) vs BDE(O−H) of the O−H bond formed.

BDE(O−H) of the HAT reaction product. To calibrate this relationship, a line was fit to the plot of rate constants (log k_2) of similar compounds whose BDE(O−H) values are determined experimentally or calculated by DFT methods. Based on this plot (Figure 4), BDEs of 85 and 89 kcal mol^{-1} are predicted for $Mn^{III}(HO{-}H)(ttppc)$ and $Fe^{III}(HO{-}H)$-(ttppc) (**2**), respectively. A similar linear correlation was obtained when the log k_2 versus BDE for 4-H-2,6-DTBP was plotted (Figure S10); however, a slightly lower BDE(O−H) value (~87 kcal mol^{-1}) was predicted for $Fe^{III}(HO{-}H)(ttppc)$ (**2**) using this substrate.

Computational Studies on the HAT Mechanism. Density functional theory (DFT) calculations were done using extensively tested and benchmarked methods, which have been shown to reproduce experimental BDEs within two kcal mol^{-1}.[59−61] We began by calculating the reaction mechanism of $Fe^{IV}(OH)(ttppc)$ (**1**) and $Mn^{IV}(OH)(ttppc)$ with the 4-H-2,6-DTBP substrate. Starting with the reactants, both complexes are charge neutral and were studied with the complete ttppc ligand included with odd (for Fe) or even (for Mn) multiplicity. The $[Fe^{IV}(OH)(ttppc)]$ complex is in a triplet spin ground state with the quintet and singlet spin states of ΔG = 3.7 and 15.4 kcal mol^{-1} higher in energy (Table S8). With manganese as the central metal ion, the ground state is the quartet spin state, while the doublet and sextet spin states are ΔE + ZPE = 21.3 and 8.0 kcal mol^{-1} higher (Table S10). The group spin densities of $^3[Fe(OH)(ttppc)]$ indicate approximately three unpaired electrons on the iron (ρ_{FeOH} = 2.79) antiferromagnetically coupled to one unpaired electron on the ttppc ligand (ρ_{tpppc} = −0.80) in an a_{2u} type orbital. These spin densities are more consistent with the $^3[Fe^{III}(OH)(ttppc^{+\bullet})]$ valence tautomer. This configuration differs from the cytochrome P450s, which, in almost all cases, is calculated to exhibit a $^3[Fe^{IV}(OH)(heme)]$ as the ground state.[22,62] We attempted to calculate the energy difference between the $Fe^{III}(OH)(ttppc^{+\bullet})$ and the $Fe^{IV}(OH)(ttppc)$ structures by swapping the molecular orbitals to obtain a structure with triplet spin configuration $\delta_{x^2-y^2}^2\,\pi^*_{xz}{}^1\,\pi^*_{yz}{}^1\,\sigma^*_{z^2}{}^0\,a_{1u}{}^2\,a_{2u}{}^2$, designated as $^3[Fe^{IV}(OH)(ttppc)]$. Unfortunately, however, during the SCF convergence the state relaxed back to the $^3[Fe^{III}(OH)(ttppc^{+\bullet})]$ state. The ground state calculations for the manganese complex gives spin densities consistent with a similar description, i.e., $^4[Mn^{III}(OH)(ttppc^{+\bullet})]$. The bond distances from the DFT optimized structures for $^3[Fe^{III}(OH)$-$(ttppc^{+\bullet})]$ (Figure S11, Table S2) and $^4[Mn^{III}(OH)(ttppc^{+\bullet})]$ (Figure S12, Table S3), as well as the reaction products $^4[Fe^{III}(H_2O)(ttppc)]$ (Figure S13, Table S4) and $^3[Mn^{III}(H_2O)(ttppc)]$ (Figure S14, Table S5), are all in good agreement with the experimentally obtained bond distances from the X-ray crystal structures of these complexes. While the DFT-optimized structures for **1** and the Mn analog suggest a metal(III)(corrole$^{+\bullet}$) structure, a definitive electronic structure assignment cannot be made from the available structural and spectroscopic data.

The hydrogen atom transfer from the *para*-H 2,6-DTBP to $Fe^{IV}(OH)(ttppc)$ and $Mn^{IV}(OH)(ttppc)$ complexes was investigated, and the transition state structures are given in Figure 5. The reaction is concerted with a single hydrogen atom abstraction to form water and phenoxyl radical. We find

DOI: 10.1021/acs.inorgchem.9b02923
Inorg. Chem. XXXX, XXX, XXX−XXX

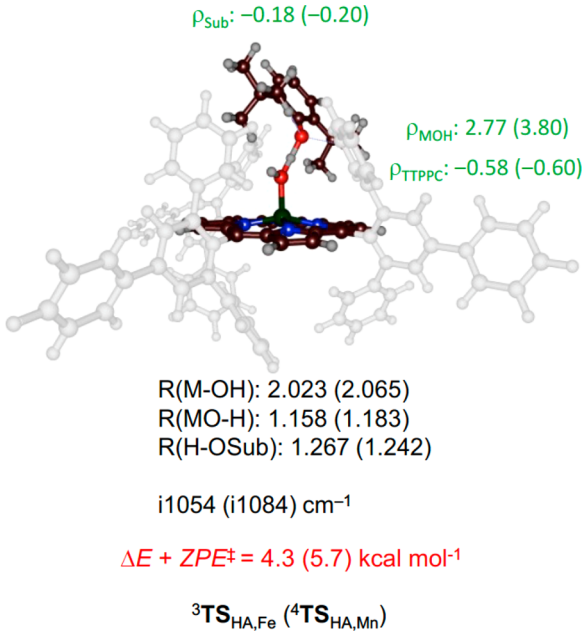

Figure 5. UB3LYP/BS2 optimized transition state geometries in solvent for the hydrogen atom abstraction from *para*-H-2,6-DTBP by $Fe^{IV}(OH)$(ttppc) and $Mn^{IV}(OH)$(ttppc). Bond lengths are in angstroms, and energies contain zero-point energy and solvent corrections.

hydrogen atom abstraction barriers of ΔE + $ZPE^{‡}$ = 4.3 and 5.7 kcal mol^{-1} for the $Fe^{IV}OH$ and $Mn^{IV}OH$ complexes, respectively (Figure S15a, Tables S8 and S10). These barriers are low and hence predict a fast chemical reaction. The difference in HAT barrier height for the $Fe^{IV}(OH)$ versus $Mn^{IV}(OH)$ complexes implicates a rate enhancement of about a factor of 10 for iron with respect to manganese from transition state theory at 298 K, which is reasonably close to the experimentally reported rate differences for this phenol (Table 2).

Geometrically, the transition states are relatively central with almost equal FeO−H versus H−OPh and MnO−H versus H−OPh distances. In particular, short FeO−H/MnO−H distances of 1.158/1.183 Å are found, while the H−O distance with the phenol is 1.267/1.242 Å. Consequently, the iron and manganese structures are very similar. The transition states are early and have an electronic structure close to the reactants, with only about 20% charge-transfer (ρ_{Sub} = −0.18/−0.20 in $^{3}TS_{HA,Fe}$/$^{4}TS_{HA,Mn}$). These results match the Hammett and Marcus plots reported above that excluded a separation of proton and electron transfer through either ET/PT or PT/ET pathways. Indeed, the electron transfer is simultaneous with proton transfer and indicates an HAT mechanism for the reaction. These spin and charge distributions in the transition states match those calculated previously for desaturation reactions by CYPs.[26,63]

To examine the contribution of the secondary coordination sphere effects of the sterically hindered ligand ttppc (5,10,15-tris(2,4,6-triphenyl)phenyl corrole) on the HAT reaction, we also ran transition state calculations with a hypothetical bare corrole, in which the (2,4,6-triphenyl)phenyl substituents on the 5,10,15- positions were removed and replaced with hydrogen atoms. Based on the potential energy landscape for the HAT reaction (Tables S12 and S14), the barrier drops considerably by 3.6 kcal mol^{-1} for ^{3}[Fe(OH)(corrole)] and by 5.3 kcal mol^{-1} for ^{4}[Mn(OH)(corrole)] (Figure S15b). The second-coordination sphere effect of the bulky phenyl groups appears to increase the HAT barrier and facilitate the direct observation of these kinetically transient chemical steps.

Calculation of Bond Dissociation Energies (BDEs) from Density Functional Theory (DFT). Bond dissociation energies (BDE_{OH}) were calculated from the following reaction of $M^{III}(H_2O)(L) \rightarrow M^{IV}(OH)(L) + H^{\bullet} + BDE_{OH}$ and taken as the energy difference of the electron affinity (EA) of the metal(IV)-hydroxide complex, the experimental ionization energy of a hydrogen atom (IE_H),[64] and the acidity (ΔG_{acid}) of the metal(III)-aquo complex (Figure S16) in their respective solvents (toluene for Fe and benzene for Mn). Our calculated BDE_{OH} values (with ZPE included) match the predicted values well, with BDE_{OH} ($Mn^{III}(H_2O)$(ttppc)) = 83.7 kcal mol^{-1} (in benzene) and BDE_{OH} ($Fe^{III}(H_2O)$(ttppc)) = 88.5 kcal mol^{-1} (in toluene) (Tables S19 and S20). The difference between these two values comes from a larger electron affinity of the iron(IV)-hydroxo complex (by 12.1 kcal mol^{-1}), which is partially canceled by a larger acidity (by 7.3 kcal mol^{-1}) of the iron(III)-aquo complex. This relative reactivity for directly analogous Fe versus Mn complexes has been similarly observed in comparisons of $Fe^{IV}(O)$ versus $Mn^{IV}(O)$ nonheme complexes, where $Fe^{IV}(O)$ species are much more reactive toward HAT substrates, due to their more positive redox potentials.[65,66] Similarly, for porphyrin and porphyrin-type complexes, $Fe^{IV}(O)(porphyrin^{\bullet+})$ species have been shown to be much more reactive toward HAT reactions versus the analogous $Mn^{V}(O)$ species in the same ligand environment.[3] In contrast, previous thermodynamic analysis of H atom transfer reactions of $Mn^{V}(O)$ versus $Cr^{V}(O)$ corrolazines revealed that the basicity of the $M^{IV}(O)$ (M = Mn, Cr) intermediate controls the H atom transfer reactivity for these reactions.[67] In the case of the H atom transfer reactions of $M^{IV}(OH)$(ttppc) (M = Fe, Mn) studied here, the larger calculated redox potential of the $Fe^{IV}(OH)$ complex seems to have a significant effect on the faster H atom transfer reactivity in comparison to $Mn^{IV}(OH)$(ttppc).

CONCLUSION

The hydrogen atom transfer reactivity of $Fe^{IV}(OH)$(ttppc) (**1**), a protonated Cpd-II analog, was described. It is capable of the rapid oxidation of phenol derivatives by H atom abstraction of the O−H bond and is more reactive than the other high-valent metal-hydroxo oxidants and the weakly oxidizing $Fe^{IV}(O)$(TMC) complexes given in Table 2 as tested against the same substrates. It also reacts more rapidly than the analogous $Mn^{IV}(OH)$(ttppc) complex, providing a direct comparison of the oxidizing power of Fe(OH) versus Mn(OH) species at the same oxidation level and in identical ligand environments. The final HAT product, $Fe^{III}(H_2O)$-(ttppc), was also definitively characterized by XRD.

The kinetic analyses and computational studies provide strong support for a mechanism of phenol oxidation by **1**, and its Mn analog, that involves a concerted, rate-determining HAT step. The calculations suggest a modest amount of charge transfer in the transition state, and this finding is in line with the weak Hammett and Marcus plot slopes. A plot of BDE(O−H) values for M(O(H)) complexes versus log k_2 for the oxidation of 4-Me-2,6-di-*tert*-butyl phenol is linear and provides a means to estimate the BDE(O−H) values for the $Fe^{III}(H_2O)$ and $Mn^{III}(H_2O)$ ttppc complexes from kinetics data. These estimated values are BDE(Fe^{III}(H**O−H**)) = ∼89

DOI: 10.1021/acs.inorgchem.9b02923
Inorg. Chem. XXXX, XXX, XXX−XXX

kcal mol^{-1} and BDE(Mn^{III}(H**O**−**H**)) = ∼85 kcal mol^{-1}, and DFT calculations fully support these values. The estimated BDE(O−H) for $Fe^{III}(H_2O)$(ttppc) is strikingly similar to the BDE(O−H) recently reported for the $Fe^{III}(H_2O)$ form of CYP158 (90 kcal mol^{-1}).[27] However, it should be noted that the BDE(O−H) calculations here are ±2 kcal mol^{-1} at best from the error in DFT calculations and kinetic measurements. Taken together, these data suggest that **1** is a viable model for protonated Cpd-II in CYP from both a structural and thermodynamic perspective, although the electronic structure of **1** may be closer to Fe^{III}(OH)(corrole$^{+\bullet}$), as opposed to Fe^{IV}(OH)(corrole).

The BDE(O−H) values for the $Fe^{III}(H_2O)$ and $Mn^{III}(H_2O)$ complexes align with the relative HAT reactivity exhibited by **1** and the Mn analog and suggest that it is the overall thermodynamic driving force for these reactions, determined by the BDE(O−H) values, that is a key factor in controlling the reaction rates of phenol oxidation. However, examination of the log k_2 versus the phenol BDE(O−H) plots for **1** and the Mn analog show that **1** is much more reactive toward the electron-rich phenols but is only modestly more reactive toward the stronger O−H bond substrates. In fact, the relative reactivities for Fe versus Mn should invert with substrates that have O−H bonds much stronger than the 83 kcal mol^{-1} reported for the *para*-H derivative. This hypothetical switch in relative reactivities, as expressed in the different slopes of log k_2 versus BDE(OH) for Fe and Mn, suggest that the BDE(O−H) of the metal-bound water ligand, and hence the thermodynamics of the overall HAT reaction, are not the only predictors of efficient H atom transfer reactivity for a high-valent metal-oxo/hydroxo species.

The Fe^{IV}(OH) complex **1** is capable of H atom abstraction, as shown with the phenols in this study, and is also capable of hydroxyl radical transfer to carbon radicals to give hydroxylated product as seen in the model "rebound" reactions described previously.[29] These findings may give some insight regarding the selection of iron, as opposed to other redox-active, earth-abundant metals such as manganese, as the metal of choice in heme monoooxygenases. The iron center appears to be an efficient and versatile oxidant in a variety of oxidation and protonation states.

EXPERIMENTAL SECTION

General Materials and Methods. All chemicals were purchased from commercial sources and used without further purification unless otherwise stated. Reactions involving inert atmosphere were performed under Ar using standard Schlenk techniques or in an N_2-filled drybox. Toluene, dichloromethane, acetonitrile, and diethyl ether were purified via a Pure-Solv solvent purification system from Innovative Technologies, Inc. Benzene, ethyl acetate, and fluorobenzene were obtained from commercial sources. Deuterated solvents for NMR were purchased from Cambridge Isotope Laboratories, Inc. (Tewksbury, MA). The 4-X-2,6-di-*tert*-butyl-phenol derivatives were recrystallized twice in ethanol (X = OMe, Me), acetonitrile (X = Et, Ac), or *n*-pentane (X = H) and dried under vacuum. The monodeuterated 4-OMe-2,6-di-*tert*-butylphenol was synthesized using a previously published procedure.[68] Fe^{IV}(OH)(ttppc) was synthesized and purified as previously reported.[29] The dark red complex $Fe^{III}(OEt_2)_2$(ttppc) was synthesized by reduction of Fe^{IV}(Cl)(ttppc), following a previously published report.[29]

Instrumentation. Kinetics and other UV−vis measurements were performed on a Hewlett-Packard Agilent 8453 diode-array spectrophotometer with a 3.5 mL quartz cuvette (path length = 1 cm). For reactions with total reaction time of <10 s, stopped-flow experiments were carried out using a HiTech SHU-61SX2 (TgK Scientific Ltd.) stopped-flow spectrophotometer with a xenon light source and Kinetic Studio software. ^{1}H NMR spectra were recorded on a Bruker Avance 400 MHz NMR spectrometer at 298 K and referenced against residual solvent proton signals. Electron paramagnetic resonance (EPR) spectra were recorded with a Bruker EMX spectrometer equipped with a Bruker ER 041 X G microwave bridge and a continuous-flow liquid helium cryostat (ESR900) coupled to an Oxford Instruments TC503 temperature controller for low temperature data collection. Laser desorption ionization mass spectrometry (LDI-MS) was conducted on a Bruker Autoflex III MALDI ToF/ToF instrument (Billerica, MA) equipped with a nitrogen laser at 335 nm using an MTP 384 ground steel target plate. The instrument was calibrated using peptide standards of known molecular weights. Gas chromatography (GC-FID) was carried out on an Agilent 6890N gas chromatograph fitted with a DB-5 5% phenylmethyl siloxane capillary column (30 m × 0.32 mm × 0.25 μm) and equipped with a flame-ionization detector. Elemental analysis was performed at Atlantic Microlab, Inc., Norcross, GA. Cyclic voltammetry was performed on an EG&G Princeton Applied Research potentiostat/galvanostat model 263A with a three-electrode system consisting of a glassy carbon working electrode, a $Ag/AgNO_3$ nonaqueous reference electrode (0.01 M $AgNO_3$ with 0.1 M Bu_4NPF_6 in CH_3CN), and a platinum wire counter electrode. Potentials were referenced using an external ferrocene standard. Scans were run under an Ar or N_2 atmosphere at 23 °C using Bu_4NPF_6 (0.1 M) as the supporting electrolyte.

$Fe^{III}(H_2O)$(ttppc) (2). Distilled H_2O (0.5 mL) was added to a solution of $Fe^{III}(OEt_2)_2$(ttppc) (100 mg) in fluorobenzene (2 mL). Vapor diffusion of pentane to this biphasic solution led to the slow formation of dark red blocks (55 mg, 56% yield) after 1 week. UV−vis (C_6H_6) λ_{max}, nm ($\varepsilon \times 10^4$ M^{-1} cm^{-1}): 344 (3.29), 429 (7.27), 578 (1.35), 764 (0.24). ^{1}H NMR (400 MHz, benzene-d_6): 35.1 (s, br), 12.4 (s, br), 12.3 (s, br), 10.8 (s, br), 8.3 (s, br), 6.0 (s, br), 4.98 (s, br), 4.66 (s, br), −19.0 (s, br), −35.1 (s, br), −61.6 (s, br), −69.0 (s, br) δ (ppm). IR (KBr): 3580 (w, O−H), 3512 (vw, O−H), 3055 (m), 3028 (m), 1593 (s), 1556 (w), 1491 (s), 1443 (m), 1424 (w), 1394 (w), 1362 (w), 1332 (m), 1296 (m), 1214 (s), 1180 (w), 1154 (m), 1075 (m), 1045 (sh), 1020 (s), 984 (s), 916 (w), 885 (s), 851 (w), 821 (w), 794 (m), 750 (vs), 695 (vs), 637 (m), 609 (w), 574 (m), 537 (m), 499 (m), 443 (w). LDI-MS (m/z): isotopic cluster centered at 1264.6 ([M − H_2O]$^+$). Anal. calcd for $C_{91}H_{59}N_4Fe{\cdot}H_2O{\cdot}2C_6H_5F$: C, 81.33; H, 5.07; N, 3.91. Found: C, 81.53; H, 4.80; N, 4.05. μ_{eff} = 3.6(1) μ_B (Evans method). EPR: g = 4.29 (16 K).

Reaction of Fe^{IV}(OH)(ttppc) with 2,4-di-*tert*-Butylphenol: Product Analysis. Under an inert atmosphere, a solution of Fe^{IV}(OH)(ttppc) in benzene (2.1 mM, 500 μL) was combined with 2,4-di-*tert*-butylphenol (0.132 mmol, 126 equiv), and 3.4 mg of eicosane (6 mM) as an internal standard. The reaction mixture was stirred and monitored by UV−vis spectroscopy, which showed rapid and complete conversion of Fe^{IV}(OH)(ttppc)(**1**) to $Fe^{III}(H_2O)$-(ttppc) (**2**). An aliquot of the reaction mixture was analyzed by GC-FID. The phenol oxidation product 3,3′,5,5′-tetra-*tert*-butyl-(1,1′-biphenyl)-2,2′-diol was identified by GC in comparison with an authentic sample and quantified by integration of the peak and comparison with a calibration curve constructed with eicosane. The analysis was performed in triplicate. The average yield was equal to 67(1)% based on the reaction stoichiometry of 0.5 equiv of phenol oxidation product per 1.0 equiv of Fe^{IV}(OH)(ttppc).

Kinetics. To a solution of Fe^{IV}(OH)(ttppc) (15 μM) in toluene, varying amounts of 4-X-2,6-di-*tert*-butylphenol (X = OMe, Me, Et, H, Ac) (0.1−3.8 mM) in toluene were added to start the reaction. The spectral changes showed isosbestic conversion of Fe^{IV}(OH)(ttppc) to $Fe^{III}(H_2O)$(ttppc). The pseudo-first-order rate constants, k_{obs}, for these reactions were obtained through nonlinear least-squares fitting of the plots of absorbance at 575 nm (Abs_t) versus time (t) over 5 half-lives according to the equation $Abs_t = Abs_f + (Abs_0 - Abs_f)\exp(-k_{obs}t)$, where Abs_0 and Abs_f are the initial and final absorbance, respectively. Second-order rate constants (k_2) were obtained from the slope of the best-fit line from a plot of k_{obs} versus phenol concentration.

DOI: 10.1021/acs.inorgchem.9b02923
Inorg. Chem. XXXX, XXX, XXX−XXX

X-ray Crystallography. All reflection intensities for **2** were measured at 110(2) K using a SuperNova diffractometer (equipped with an Atlas detector) with Cu Kα radiation (λ = 1.54178 Å) under the program CrysAlisPro (version 1.171.39.29c, Rigaku OD, 2017). The same program was used to refine the cell dimensions and for data reduction. The structure was solved with the program SHELXS-2014/7 and refined on F^2 with SHELXL-2014/7.[69] The temperature of the data collection was controlled using the system Cryojet (manufactured by Oxford Instruments). An analytical numeric absorption correction method was used involving a multifaceted crystal model based on expressions derived elsewhere.[70] The H atoms were placed at calculated positions using the instructions AFIX 43 with isotropic displacement parameters having values 1.2 Ueq of the attached C atoms. The crystal lattice contains disordered and/or partially occupied lattice solvent molecules (C_6H_5F and C_5H_{12}). Their contributions were removed from the final refinement using the SQUEEZE program. The crystallographic data for $Fe^{III}(H_2O)$(ttppc) are summarized in Table S6.

Computational Modeling. Calculations on the complexes Fe^{IV}(OH)(ttppc) and Mn^{IV}(OH)(ttppc) and their reactions with *para*-H-2,6-DTBP included all atoms for both metal complex and phenol. Geometry optimizations, constraint geometry scans, and vibrational frequencies were calculated with DFT in the Gaussian-09 software package.[71] We utilized the unrestricted B3LYP hybrid density functional method[72,73] in combination with an LANL2DZ basis set[74,75] on iron/manganese (with core potential) and 6-31G on the rest of the atoms (H, C, N, O), e.g., basis set BS1. Single points using the LACV3P+ (with core potential) on Fe/Mn and 6-311+G* on the rest of the atoms were done to correct the energies, e.g., basis set BS2. The continuum polarized conductor model with a dielectric constant mimicking toluene was applied to the system during the geometry optimizations and frequency calculations.[76] Single point energy calculations were also done in benzene, e.g., basis set BS3, for the BDE determination of $Mn^{III}(H_2O)$(ttppc) to match the experimental conditions (Table S20). We initially optimized a reactant complex of substrate and metal(IV)-hydroxo species in close proximity and followed the pathway for H transfer through a constrained geometry scan. Subsequently, the maximum in energy of these scans was subjected to a full transition state search and the obtained transition state was characterized with a frequency calculation that gave an imaginary frequency for the correct mode. These transition states were shown to be connected to reactants and products through an intrinsic reaction coordinate (IRC) scan. As in some cases, the transition states energies were lower than those of the original reactant complexes, so the latter were reoptimized from the final points of the IRCs, which gave slightly more stable isomers. These methods were used in previous studies and were shown to predict the correct spin-state orderings and barrier heights of reaction mechanisms.[26,77,78] The calculations of the BDE(O−H) values are described in the Supporting Information (Tables S19 and S20).

■ ASSOCIATED CONTENT

Supporting Information

The Supporting Information is available free of charge at https://pubs.acs.org/doi/10.1021/acs.inorgchem.9b02923.

EPR spectra, kinetics data, single-crystal X-ray crystallography analysis, DFT optimized structures, calculation of BDEs, computational tables with group spin densities, charges, and absolute and relative energies of all structures, as well as Cartesian coordinates of optimized geometries (PDF)

Accession Codes

CCDC 1836730 contains the supplementary crystallographic data for this paper. These data can be obtained free of charge via www.ccdc.cam.ac.uk/data_request/cif, or by emailing data_request@ccdc.cam.ac.uk, or by contacting The Cambridge Crystallographic Data Centre, 12 Union Road, Cambridge CB2 1EZ, UK; fax: +44 1223 336033.

■ AUTHOR INFORMATION

Corresponding Authors

*E-mail: dpg@jhu.edu. (D.P.G.)
*E-mail: sam.devisser@manchester.ac.uk. (S.P.V.)

ORCID

Jan Paulo T. Zaragoza: 0000-0002-2583-6571
Maxime A. Siegler: 0000-0003-4165-7810
Sam P. de Visser: 0000-0002-2620-8788
David P. Goldberg: 0000-0003-4645-1045

Notes

The authors declare no competing financial interest.

■ ACKNOWLEDGMENTS

The authors would like to thank the NIH (GM101153) (D.P.G.) for the financial support provided for this research. M.Q.E.M. thanks the Ministry of Higher Education Malaysia and Islamic Science University of Malaysia (USIM) for a studentship. J.P.T.Z. thanks JHU for the Glen E. Meyer '39 Fellowship.

■ REFERENCES

(1) Zaragoza, J. P. T.; Goldberg, D. P. Dioxygen Binding and Activation Mediated by Transition Metal Porphyrinoid Complexes. In *Dioxygen-dependent Heme Enzymes*; Ikeda-Saito, M., Raven, E., Eds.; The Royal Society of Chemistry, 2019; pp 1−36.

(2) Sahu, S.; Goldberg, D. P. Activation of Dioxygen by Iron and Manganese Complexes: A Heme and Nonheme Perspective. *J. Am. Chem. Soc.* **2016**, *138*, 11410−11428.

(3) Baglia, R. A.; Zaragoza, J. P. T.; Goldberg, D. P. Biomimetic Reactivity of Oxygen-Derived Manganese and Iron Porphyrinoid Complexes. *Chem. Rev.* **2017**, *117*, 13320−13352.

(4) Sacramento, J. J. D.; Goldberg, D. P. Factors Affecting Hydrogen Atom Transfer Reactivity of Metal−Oxo Porphyrinoid Complexes. *Acc. Chem. Res.* **2018**, *51*, 2641−2652.

(5) Engelmann, X.; Monte-Pérez, I.; Ray, K. Oxidation Reactions with Bioinspired Mononuclear Non-Heme Metal−Oxo Complexes. *Angew. Chem., Int. Ed.* **2016**, *55*, 7632−7649.

(6) Nam, W.; Lee, Y.-M.; Fukuzumi, S. Tuning Reactivity and Mechanism in Oxidation Reactions by Mononuclear Nonheme Iron(IV)-Oxo Complexes. *Acc. Chem. Res.* **2014**, *47*, 1146−1154.

(7) McDonald, A. R.; Que, L., Jr. High-valent nonheme iron-oxo complexes: Synthesis, structure, and spectroscopy. *Coord. Chem. Rev.* **2013**, *257*, 414−428.

(8) Ortiz de Montellano, P. R. Hydrocarbon Hydroxylation by Cytochrome P450 Enzymes. *Chem. Rev.* **2010**, *110*, 932−948.

(9) Poulos, T. L. Heme Enzyme Structure and Function. *Chem. Rev.* **2014**, *114*, 3919−3962.

(10) Rittle, J.; Green, M. T. Cytochrome P450 Compound I: Capture, Characterization, and C-H Bond Activation Kinetics. *Science* **2010**, *330*, 933−937.

(11) Huang, X.; Groves, J. T. Beyond ferryl-mediated hydroxylation: 40 years of the rebound mechanism and C−H activation. *JBIC, J. Biol. Inorg. Chem.* **2017**, *22*, 185−207.

(12) Makris, T. M.; von Koenig, K.; Schlichting, I.; Sligar, S. G. The status of high-valent metal oxo complexes in the P450 cytochromes. *J. Inorg. Biochem.* **2006**, *100*, 507−518.

(13) Denisov, I. G.; Makris, T. M.; Sligar, S. G.; Schlichting, I. Structure and Chemistry of Cytochrome P450. *Chem. Rev.* **2005**, *105*, 2253−2278.

(14) Rettie, A. E.; Sheffels, P. R.; Korzekwa, K. R.; Gonzalez, F. J.; Philpot, R. M.; Baillie, T. A. CYP4 Isoenzyme Specificity and the

DOI: 10.1021/acs.inorgchem.9b02923
Inorg. Chem. XXXX, XXX, XXX−XXX

Relationship between ω-Hydroxylation and Terminal Desaturation of Valproic Acid. *Biochemistry* **1995**, *34*, 7889−7895.
(15) Rettie, A. E.; Boberg, M.; Rettenmeier, A. W.; Baillie, T. A. Cytochrome P-450-catalyzed desaturation of valproic acid in vitro. Species differences, induction effects, and mechanistic studies. *J. Biol. Chem.* **1988**, *263*, 13733−13738.
(16) Rettie, A. E.; Rettenmeier, A. W.; Howald, W. N.; Baillie, T. A. Cytochrome P-450-catalyzed formation of Δ^4-VPA, a toxic metabolite of valproic acid. *Science* **1987**, *235*, 890−893.
(17) Guengerich, F. P.; Kim, D. H. Enzymic oxidation of ethyl carbamate to vinyl carbamate and its role as an intermediate in the formation of 1,N^6-ethenoadenosine. *Chem. Res. Toxicol.* **1991**, *4*, 413−421.
(18) Nagata, K.; Liberato, D. J.; Gillette, J. R.; Sasame, H. A. An unusual metabolite of testosterone. 17 β-Hydroxy-4,6-androstadiene-3-one. *Drug Metab. Dispos.* **1986**, *14*, 559−565.
(19) Guan, X.; Fisher, M. B.; Lang, D. H.; Zheng, Y.-M.; Koop, D. R.; Rettie, A. E. Cytochrome P450-dependent desaturation of lauric acid: isoform selectivity and mechanism of formation of 11-dodecenoic acid. *Chem. Biol. Interact.* **1998**, *110*, 103−121.
(20) Rude, M. A.; Baron, T. S.; Brubaker, S.; Alibhai, M.; Del Cardayre, S. B.; Schirmer, A. Terminal Olefin (1-Alkene) Biosynthesis by a Novel P450 Fatty Acid Decarboxylase from *Jeotgalicoccus* Species. *Appl. Environ. Microbiol.* **2011**, *77*, 1718−1727.
(21) Liu, Y.; Wang, C.; Yan, J.; Zhang, W.; Guan, W.; Lu, X.; Li, S. Hydrogen peroxide-independent production of α-alkenes by OleTJE P450 fatty acid decarboxylase. *Biotechnol. Biofuels* **2014**, *7*, 28−39.
(22) Faponle, A. S.; Quesne, M. G.; de Visser, S. P. Origin of the Regioselective Fatty-Acid Hydroxylation versus Decarboxylation by a Cytochrome P450 Peroxygenase: What Drives the Reaction to Biofuel Production? *Chem. - Eur. J.* **2016**, *22*, 5478−5483.
(23) Belcher, J.; McLean, K. J.; Matthews, S.; Woodward, L. S.; Fisher, K.; Rigby, S. E. J.; Nelson, D. R.; Potts, D.; Baynham, M. T.; Parker, D. A.; Leys, D.; Munro, A. W. Structure and Biochemical Properties of the Alkene Producing Cytochrome P450 OleTJE (CYP152L1) from the *Jeotgalicoccus sp.* 8456 Bacterium. *J. Biol. Chem.* **2014**, *289*, 6535−6550.
(24) Grant, J. L.; Mitchell, M. E.; Makris, T. M. Catalytic strategy for carbon−carbon bond scission by the cytochrome P450 OleT. *Proc. Natl. Acad. Sci. U. S. A.* **2016**, *113*, 10049−10054.
(25) Hsieh, C. H.; Huang, X.; Amaya, J. A.; Rutland, C. D.; Keys, C. L.; Groves, J. T.; Austin, R. N.; Makris, T. M. The Enigmatic P450 Decarboxylase OleT Is Capable of, but Evolved To Frustrate, Oxygen Rebound Chemistry. *Biochemistry* **2017**, *56*, 3347−3357.
(26) Pickl, M.; Kurakin, S.; Cantú Reinhard, F. G.; Schmid, P.; Pöcheim, A.; Winkler, C. K.; Kroutil, W.; de Visser, S. P.; Faber, K. Mechanistic Studies of Fatty Acid Activation by CYP152 Peroxygenases Reveal Unexpected Desaturase Activity. *ACS Catal.* **2019**, *9*, 565−577.
(27) Mittra, K.; Green, M. T. Reduction Potentials of P450 Compounds I and II: Insight into the Thermodynamics of C−H Bond Activation. *J. Am. Chem. Soc.* **2019**, *141*, 5504−5510.
(28) Hayashi, Y.; Yamazaki, I. The oxidation-reduction potentials of compound I/compound II and compound II/ferric couples of horseradish peroxidases A2 and C. *J. Biol. Chem.* **1979**, *254*, 9101−9106.
(29) Zaragoza, J. P. T.; Yosca, T. H.; Siegler, M. A.; Moënne-Loccoz, P.; Green, M. T.; Goldberg, D. P. Direct Observation of Oxygen Rebound with an Iron-Hydroxide Complex. *J. Am. Chem. Soc.* **2017**, *139*, 13640−13643.
(30) Ganguly, S.; Giles, L. J.; Thomas, K. E.; Sarangi, R.; Ghosh, A. Ligand Noninnocence in Iron Corroles: Insights from Optical and X-ray Absorption Spectroscopies and Electrochemical Redox Potentials. *Chem. - Eur. J.* **2017**, *23*, 15098−15106.
(31) Ganguly, S.; McCormick, L. J.; Conradie, J.; Gagnon, K. J.; Sarangi, R.; Ghosh, A. Electronic Structure of Manganese Corroles Revisited: X-ray Structures, Optical and X-ray Absorption Spectroscopies, and Electrochemistry as Probes of Ligand Noninnocence. *Inorg. Chem.* **2018**, *57*, 9656−9669.
(32) Weitz, A. C.; Mills, M. R.; Ryabov, A. D.; Collins, T. J.; Guo, Y.; Bominaar, E. L.; Hendrich, M. P. A Synthetically Generated $LFe^{IV}OH_n$ Complex. *Inorg. Chem.* **2019**, *58*, 2099−2108.
(33) Drummond, M. J.; Ford, C. L.; Gray, D. L.; Popescu, C. V.; Fout, A. R. Radical Rebound Hydroxylation Versus H-Atom Transfer in Non-Heme Iron(III)-Hydroxo Complexes: Reactivity and Structural Differentiation. *J. Am. Chem. Soc.* **2019**, *141*, 6639−6650.
(34) Xu, N.; Powell, D. R.; Richter-Addo, G. B. Nitrosylation in a Crystal: Remarkable Movements of Iron Porphyrins Upon Binding of Nitric Oxide. *Angew. Chem., Int. Ed.* **2011**, *50*, 9694−9696.
(35) Cheng, B.; Safo, M. K.; Orosz, R. D.; Reed, C. A.; Debrunner, P. G.; Scheidt, W. R. Synthesis, Structure, and Characterization of Five-Coordinate Aquo(octaethylporphinato)iron(III) Perchlorate. *Inorg. Chem.* **1994**, *33*, 1319−1324.
(36) Ohgo, Y.; Chiba, Y.; Hashizume, D.; Uekusa, H.; Ozeki, T.; Nakamura, M. Novel spin transition between S = 5/2 and S = 3/2 in highly saddled iron(III) porphyrin complexes at extremely low temperatures. *Chem. Commun.* **2006**, 1935−1937.
(37) Ellis, W. C.; Tran, C. T.; Roy, R.; Rusten, M.; Fischer, A.; Ryabov, A. D.; Blumberg, B.; Collins, T. J. Designing Green Oxidation Catalysts for Purifying Environmental Waters. *J. Am. Chem. Soc.* **2010**, *132*, 9774−9781.
(38) Ghosh, A.; Ryabov, A. D.; Mayer, S. M.; Horner, D. C.; Prasuhn, D. E.; Sen Gupta, S.; Vuocolo, L.; Culver, C.; Hendrich, M. P.; Rickard, C. E. F.; Norman, R. E.; Horwitz, C. P.; Collins, T. J. Understanding the Mechanism of H^+-Induced Demetalation as a Design Strategy for Robust Iron(III) Peroxide-Activating Catalysts. *J. Am. Chem. Soc.* **2003**, *125*, 12378−12379.
(39) Simkhovich, L.; Goldberg, I.; Gross, Z. Iron(III) and Iron(IV) Corroles: Synthesis, Spectroscopy, Structures, and No Indications for Corrole Radicals. *Inorg. Chem.* **2002**, *41*, 5433−5439.
(40) Simkhovich, L.; Mahammed, A.; Goldberg, I.; Gross, Z. Synthesis and Characterization of Germanium, Tin, Phosphorus, Iron, and Rhodium Complexes of Tris(pentafluorophenyl)corrole, and the Utilization of the Iron and Rhodium Corroles as Cyclopropanation Catalysts. *Chem. - Eur. J.* **2001**, *7*, 1041−1055.
(41) Zaragoza, J. P. T.; Siegler, M. A.; Goldberg, D. P. A Reactive Manganese(IV)−Hydroxide Complex: A Missing Intermediate in Hydrogen Atom Transfer by High-Valent Metal-Oxo Porphyrinoid Compounds. *J. Am. Chem. Soc.* **2018**, *140*, 4380−4390.
(42) Blomberg, M. R. A.; Siegbahn, P. E. M. A comparative study of high-spin manganese and iron complexes. *Theor. Chem. Acc.* **1997**, *97*, 72−80.
(43) Stein, S. E.; Brown, R. L. Prediction of carbon-hydrogen bond dissociation energies for polycyclic aromatic hydrocarbons of arbitrary size. *J. Am. Chem. Soc.* **1991**, *113*, 787−793.
(44) Hansch, C.; Leo, A.; Taft, R. W. A survey of Hammett substituent constants and resonance and field parameters. *Chem. Rev.* **1991**, *91*, 165−195.
(45) Lee, J. Y.; Peterson, R. L.; Ohkubo, K.; Garcia-Bosch, I.; Himes, R. A.; Woertink, J.; Moore, C. D.; Solomon, E. I.; Fukuzumi, S.; Karlin, K. D. Mechanistic Insights into the Oxidation of Substituted Phenols via Hydrogen Atom Abstraction by a Cupric−Superoxo Complex. *J. Am. Chem. Soc.* **2014**, *136*, 9925−9937.
(46) Lucarini, M.; Pedrielli, P.; Pedulli, G. F.; Cabiddu, S.; Fattuoni, C. Bond Dissociation Energies of O−H Bonds in Substituted Phenols from Equilibration Studies. *J. Org. Chem.* **1996**, *61*, 9259−9263.
(47) Marcus, R. A.; Sutin, N. Electron transfers in chemistry and biology. *Biochim. Biophys. Acta, Rev. Bioenerg.* **1985**, *811*, 265−322.
(48) Wijeratne, G. B.; Corzine, B.; Day, V. W.; Jackson, T. A. Saturation Kinetics in Phenolic O−H Bond Oxidation by a Mononuclear Mn(III)−OH Complex Derived from Dioxygen. *Inorg. Chem.* **2014**, *53*, 7622−7634.
(49) Rice, D. B.; Wijeratne, G. B.; Burr, A. D.; Parham, J. D.; Day, V. W.; Jackson, T. A. Steric and Electronic Influence on Proton-Coupled Electron-Transfer Reactivity of a Mononuclear Mn(III)-Hydroxo Complex. *Inorg. Chem.* **2016**, *55*, 8110−8120.
(50) Sastri, C. V.; Lee, J.; Oh, K.; Lee, Y. J.; Lee, J.; Jackson, T. A.; Ray, K.; Hirao, H.; Shin, W.; Halfen, J. A.; Kim, J.; Que, L., Jr.; Shaik,

DOI: 10.1021/acs.inorgchem.9b02923
Inorg. Chem. XXXX, XXX, XXX−XXX

S.; Nam, W. Axial ligand tuning of a nonheme iron(IV)−oxo unit for hydrogen atom abstraction. *Proc. Natl. Acad. Sci. U. S. A.* **2007**, *104*, 19181−19186.
(51) Kurahashi, T.; Kikuchi, A.; Shiro, Y.; Hada, M.; Fujii, H. Unique Properties and Reactivity of High-Valent Manganese−Oxo versus Manganese−Hydroxo in the Salen Platform. *Inorg. Chem.* **2010**, *49*, 6664−6672.
(52) Yiu, D. T. Y.; Lee, M. F. W.; Lam, W. W. Y.; Lau, T.-C. Kinetics and Mechanisms of the Oxidation of Phenols by a trans-Dioxoruthenium(VI) Complex. *Inorg. Chem.* **2003**, *42*, 1225−1232.
(53) Das, P. K.; Encinas, M. V.; Steenken, S.; Scaiano, J. C. Reaction of tert-butoxy radicals with phenols. Comparison with the reactions of carbonyl triplets. *J. Am. Chem. Soc.* **1981**, *103*, 4162−4166.
(54) Finn, M.; Friedline, R.; Suleman, N. K.; Wohl, C. J.; Tanko, J. M. Chemistry of the t-Butoxyl Radical: Evidence that Most Hydrogen Abstractions from Carbon are Entropy-Controlled. *J. Am. Chem. Soc.* **2004**, *126*, 7578−7584.
(55) Massie, A. A.; Sinha, A.; Parham, J. D.; Nordlander, E.; Jackson, T. A. Relationship between Hydrogen-Atom Transfer Driving Force and Reaction Rates for an Oxomanganese(IV) Adduct. *Inorg. Chem.* **2018**, *57*, 8253−8263.
(56) Kaizer, J.; Klinker, E. J.; Oh, N. Y.; Rohde, J.-U.; Song, W. J.; Stubna, A.; Kim, J.; Münck, E.; Nam, W.; Que, L., Jr. Nonheme $Fe^{IV}O$ Complexes That Can Oxidize the C−H Bonds of Cyclohexane at Room Temperature. *J. Am. Chem. Soc.* **2004**, *126*, 472−473.
(57) Wu, X.; Seo, M. S.; Davis, K. M.; Lee, Y.-M.; Chen, J.; Cho, K.-B.; Pushkar, Y. N.; Nam, W. A Highly Reactive Mononuclear Non-Heme Manganese(IV)−Oxo Complex That Can Activate the Strong C−H Bonds of Alkanes. *J. Am. Chem. Soc.* **2011**, *133*, 20088−20091.
(58) Lansky, D. E.; Goldberg, D. P. Hydrogen Atom Abstraction by a High-Valent Manganese(V)−Oxo Corrolazine. *Inorg. Chem.* **2006**, *45*, 5119−5125.
(59) de Visser, S. P. Trends in Substrate Hydroxylation Reactions by Heme and Nonheme Iron(IV)-Oxo Oxidants Give Correlations between Intrinsic Properties of the Oxidant with Barrier Height. *J. Am. Chem. Soc.* **2010**, *132*, 1087−1097.
(60) Kumar, D.; Karamzadeh, B.; Sastry, G. N.; de Visser, S. P. What Factors Influence the Rate Constant of Substrate Epoxidation by Compound I of Cytochrome P450 and Analogous Iron(IV)-Oxo Oxidants? *J. Am. Chem. Soc.* **2010**, *132*, 7656−7667.
(61) Cantú Reinhard, F. G.; Faponle, A. S.; de Visser, S. P. Substrate Sulfoxidation by an Iron(IV)-Oxo Complex: Benchmarking Computationally Calculated Barrier Heights to Experiment. *J. Phys. Chem. A* **2016**, *120*, 9805−9814.
(62) de Visser, S. P.; Ogliaro, F.; Sharma, P. K.; Shaik, S. What Factors Affect the Regioselectivity of Oxidation by Cytochrome P450? A DFT Study of Allylic Hydroxylation and Double Bond Epoxidation in a Model Reaction. *J. Am. Chem. Soc.* **2002**, *124*, 11809−11826.
(63) Li, X.-X.; Postils, V.; Sun, W.; Faponle, A. S.; Solà, M.; Wang, Y.; Nam, W.; de Visser, S. P. Reactivity Patterns of (Protonated) Compound II and Compound I of Cytochrome P450: Which is the Better Oxidant? *Chem. - Eur. J.* **2017**, *23*, 6406−6418.
(64) Lias, S. G. Ionization Energy Evaluation in the NIST Chemistry WebBook. In *NIST Standard Reference Database Number 69*; Linstrom, P. J., Mallard, W. G., Eds.; National Institute of Standards and Technology: Gaithersburg, MD, 2005; pp 20899.
(65) Chen, J.; Cho, K.-B.; Lee, Y.-M.; Kwon, Y. H.; Nam, W. Mononuclear nonheme iron(IV)−oxo and manganese(IV)−oxo complexes in oxidation reactions: experimental results prove theoretical prediction. *Chem. Commun.* **2015**, *51*, 13094−13097.
(66) Denler, M. C.; Massie, A. A.; Singh, R.; Stewart-Jones, E.; Sinha, A.; Day, V. W.; Nordlander, E.; Jackson, T. A. Mn^{IV}-Oxo complex of a bis(benzimidazolyl)-containing N5 ligand reveals different reactivity trends for Mn^{IV}-oxo than Fe^{IV}-oxo species. *Dalton Trans.* **2019**, *48*, 5007−5021.
(67) Baglia, R. A.; Prokop-Prigge, K. A.; Neu, H. M.; Siegler, M. A.; Goldberg, D. P. Mn(V)(O) versus Cr(V)(O) Porphyrinoid Complexes: Structural Characterization and Implications for Basicity Controlling H-Atom Abstraction. *J. Am. Chem. Soc.* **2015**, *137*, 10874−10877.
(68) Kundu, S.; Miceli, E.; Farquhar, E. R.; Ray, K. Mechanism of phenol oxidation by heterodinuclear Ni Cu bis(μ-oxo) complexes involving nucleophilic oxo groups. *Dalton Trans.* **2014**, *43*, 4264−4267.
(69) Sheldrick, G. Crystal structure refinement with SHELXL. *Acta Crystallogr., Sect. C* **2015**, *71*, 3−8.
(70) Clark, R. C.; Reid, J. S. The analytical calculation of absorption in multifaceted crystals. *Acta Crystallogr., Sect. A: Found. Crystallogr.* **1995**, *51*, 887−897.
(71) Frisch, M. J.; Trucks, G. W.; Schlegel, H. B.; Scuseria, G. E.; Robb, M. A.; Cheeseman, J. R.; Scalmani, G.; Barone, V.; Mennucci, B.; Petersson, G. A.; Nakatsuji, H.; Caricato, M.; Li, X.; Hratchian, H. P.; Izmaylov, A. F.; Bloino, J.; Zheng, G.; Sonnenberg, J. L.; Hada, M.; Ehara, M.; Toyota, K.; Fukuda, R.; Hasegawa, J.; Ishida, M.; Nakajima, T.; Honda, Y.; Kitao, O.; Nakai, H.; Vreven, T.; Montgomery, J. A., Jr.; Peralta, J. E.; Ogliaro, F.; Bearpark, M.; Heyd, J. J.; Brothers, E.; Kudin, K. N.; Staroverov, V. N.; Kobayashi, R.; Normand, J.; Raghavachari, K.; Rendell, A.; Burant, J. C.; Iyengar, S. S.; Tomasi, J.; Cossi, M.; Rega, N.; Millam, J. M.; Klene, M.; Knox, J. E.; Cross, J. B.; Bakken, V.; Adamo, C.; Jaramillo, J.; Gomperts, R.; Stratmann, R. E.; Yazyev, O.; Austin, A. J.; Cammi, R.; Pomelli, C.; Ochterski, J. W.; Martin, R. L.; Morokuma, K.; Zakrzewski, V. G.; Voth, G. A.; Salvador, P.; Dannenberg, J. J.; Dapprich, S.; Daniels, A. D.; Farkas, O.; Foresman, J. B.; Ortiz, J. V.; Cioslowski, J.; Fox, D. J. *Gaussian 09*, revision A.1; Gaussian, Inc.: Wallingford, CT, 2009.
(72) Becke, A. D. Density-functional thermochemistry. III. The role of exact exchange. *J. Chem. Phys.* **1993**, *98*, 5648−5652.
(73) Lee, C.; Yang, W.; Parr, R. G. Development of the Colle-Salvetti correlation-energy formula into a functional of the electron density. *Phys. Rev. B* **1988**, *37*, 785−789.
(74) Hay, P. J.; Wadt, W. R. Ab Initio Effective Core Potentials for Molecular Calculations - Potentials for the Transition-Metal Atoms Sc to Hg. *J. Chem. Phys.* **1985**, *82*, 270−283.
(75) Francl, M. M.; Pietro, W. J.; Hehre, W. J.; Binkley, J. S.; Gordon, M. S.; DeFrees, D. J.; Pople, J. A. Self-consistent molecular orbital methods. XXIII. A polarization-type basis set for second-row elements. *J. Chem. Phys.* **1982**, *77*, 3654.
(76) Tomasi, J.; Mennucci, B.; Cammi, R. Quantum Mechanical Continuum Solvation Models. *Chem. Rev.* **2005**, *105*, 2999−3094.
(77) Kumar, S.; Faponle, A. S.; Barman, P.; Vardhaman, A. K.; Sastri, C. V.; Kumar, D.; de Visser, S. P. Long-Range Electron Transfer Triggers Mechanistic Differences between Iron(IV)-Oxo and Iron-(IV)-Imido Oxidants. *J. Am. Chem. Soc.* **2014**, *136*, 17102−17115.
(78) Yang, T.; Quesne, M. G.; Neu, H. M.; Cantú Reinhard, F. G.; Goldberg, D. P.; de Visser, S. P. Singlet versus Triplet Reactivity in an Mn(V)−Oxo Species: Testing Theoretical Predictions Against Experimental Evidence. *J. Am. Chem. Soc.* **2016**, *138*, 12375−12386.

DOI: 10.1021/acs.inorgchem.9b02923
Inorg. Chem. XXXX, XXX, XXX−XXX